

Targeting the Soleus and Quadriceps Muscles Using Powered Robotic Rehabilitation Devices and Neuromuscular Control

A Thesis Submitted in Partial Fulfillment of the
Requirements of the Renée Crown University Honors Program at
Syracuse University

Evan Ryan Tulsky

Candidate for Bachelor of Degree (B.S.)

and Renée Crown University Honors

May 2024

Copyright © Evan Ryan Tulsky May 2024

All Rights Reserved

Abstract

Rehabilitation machines can promote neurological and functional recovery. Lower limb powered exoskeletons can enhance mobility, increase muscle mass, and improve strength during gait training. Similarly, functional electrical stimulation (FES) can induce cardiovascular and neuromuscular benefits in cycling exercises. However, controlling powered machines and FES devices poses technical challenges. Firstly, humans experience neuromuscular fatigue which decreases the duration of the rehabilitation. Secondly, the variability in human dynamics are time-varying and nonlinear. Hence, adaptive control strategies are motivated to human dynamics inputs in real-time. Therefore, developing rehabilitative devices that interface effectively with humans necessitates addressing the influence of fatigue and variability in the human dynamics.

This thesis introduces control methods integrating the powered machines and neuromuscular control techniques. The control algorithms address inherent nonlinear effects in the hybrid machines, compensate for human input, and mitigate muscle fatigue. To achieve this, the proposed control designs utilize kinematic feedback to control electric motors to pedal a lower-limb cycle and interface an ankle-foot orthosis. Additionally, neuromuscular control tools such as electromyography (EMG), FES, and vibration stimuli are combined with the electric machines. Controllers are developed to safely combine the machines and neuromuscular tools with assistive technologies in clinical and community settings. Chapter 1 introduces the rationale for integrating closed-loop controllers for a motorized powered ankle-foot orthosis with electromyography is introduced. Then the combination of FES induced cycling is discussed to mitigate fatigue. Chapter 2 introduces the dynamic model for the ankle-foot orthosis for walking. The ankle-foot orthosis is modeled as a single degree-of-freedom (DoF) system. The experimental test beds for the ankle-foot exoskeleton and cycling system are described. Chapter 3 develops an extremum seeking control (ESC) for the ankle orthosis device to compute a optimal dorsiflexion perturbation angle during walking exercise. This ESC control is developed based on ground reaction measurements and soleus muscle EMG data. Additionally, a closed-loop robust feedback controller is designed to track the computed ankle perturbation. Chapter 4 combines the application of vibration stimuli to the quadriceps femoris in FES cycling. Since FES can induce discomfort and accelerate muscle fatigue, vibration stimuli can provide sensory feedback to the muscle and potentially delay fatigue during vibration experiments. Chapter 5 summarizes the contributions of the developed control methods and provides recommendations for future research directions.

Executive Summary

Neurological disorders (NDs) such as spinal cord injury (SCI) and stroke result in partial or total loss of motor and sensory functions, significantly impacting an individual's independence and quality of life [1], [2]. Restoring and improving motor function is a priority for individuals with NDs, as it is crucial in enhancing their overall well-being and daily activities [1], [3]. Rehabilitation machines can promote neurological and functional recovery.

Powered systems that physically interact with humans need to adapt their responses to ensure stability and safety. Controllers for rehabilitation robots interacting with people with neurological impairments should ensure safe human-machine interaction and seamlessly customize the assistance for participants with different functional capacities. Thus, advancing the control algorithms of rehabilitation robotic devices can accelerate their adoption in clinical settings, thereby having the potential to make a significant impact on patients' recovery.

Lower limb powered exoskeletons can enhance mobility, increase muscle mass, and improve strength during gait training. Powered exoskeletons improve range of motion, gait function, and endurance [4], [5]. Exoskeletons enable individuals with NDs to engage in overground walking or treadmill-based walking with body weight support, which helps partially offload the user's weight and is particularly beneficial for individuals with limited weight-bearing capacity [6]. However, typical robotic-assisted approaches cannot ensure people with NDs will retain gait benefits once the assistance provided by the device is removed. A technical challenge is to integrate wearable devices and their controllers during these novel gait training strategies that promote lasting gait benefits.

Similarly, functional electrical stimulation (FES) can induce cardiovascular and neuromuscular benefits in cycling exercises. FES-cycling is a rehabilitative strategy typically prescribed, wherein a voltage potential is applied to lower-limb muscles to induce controlled contractions and facilitate pedaling a cycle, either with or without motorized assistance [7]. FES-cycling has

been shown to impart cardiovascular and physiological benefits, thereby improving the quality of life for individuals with NDs [8]–[10]. In motorized FES-cycling, FES is applied to multiple muscle groups to evoke active torque complemented by the assistance of an electric motor [11]. FES-cycling is recommended for people with increased fall risks and impaired sensory feedback who are excluded from gait training or other high cardiovascular exercises. However, controlling powered machines poses technical challenges.

Firstly, humans experience neuromuscular fatigue which decreases the duration of the rehabilitation. Secondly, the variability in human dynamics are time-varying and nonlinear. Hence, adaptive control strategies are motivated to human dynamics inputs in real-time. Hence, developing rehabilitative devices that interface effectively with humans necessitates addressing the influence of fatigue and variability in the human dynamics.

This thesis introduces control methods integrating the powered machines and neuromuscular control techniques. The control algorithms address inherent nonlinear effects in the hybrid machines, compensate for human input, and mitigate muscle fatigue. To achieve this, the proposed control designs utilize kinematic feedback to control electric motors to pedal a lower-limb cycle and interface an ankle-foot orthosis. Additionally, neuromuscular control tools such as electromyography (EMG), FES, and vibration stimuli are combined with the electric machines. Controllers are developed to safely combine the machines and neuromuscular tools with assistive technologies in clinical and community settings.

Contents

Title	i
Copyright	ii
Abstract	iii
Executive Summary	iv
List of Tables	viii
List of Figures	ix
Acknowledgements	xii
1 Introduction	1
1.1 Rehabilitation with Hybrid Machines	1
1.1.1 Powered Exoskeletons for Walking with EMG	2
1.1.2 Motorized FES-Cycling with Muscle Vibration	4
2 Dynamic Models and Experimental Setup	7
2.1 Powered Ankle-Foot Orthosis System	7
2.2 Motorized FES-Cycling	10
3 Extremum Seeking Control Targeting the Soleus Muscle During Walking	14

3.1	Control Development	15
3.1.1	Extremum Seeking Control for Ankle Perturbation Trajectory Generation .	16
3.1.2	Ankle Perturbation Tracking Controller	18
3.2	Stability Analysis	19
3.3	Gait Protocol	21
3.4	Results	22
4	Influence of Vibration Stimuli on the Quadriceps Femoris Muscles During FES-Induced Cycling	26
4.1	Experimental Protocol	26
4.2	Results	28
5	Conclusion and Research Directions	33
References		35
6	Vita	42
6.1	Publications	42

List of Tables

3.1	The average terminal error, \bar{e}_T , average desired angle, \bar{Q}_d , and the percent error $\%e_T$ that represents the ratio of the terminal error to desired perturbation angle $\frac{e_T}{\bar{Q}_d}$. The average soleus muscle EMG activity \bar{S} is reported for the first 10 and last 10 perturbed steps with ESC.	23
4.1	Mean active torque, fatigue time and fatigue rate for the FES-cycling trials with and without vibration across the four subjects. The pulse width used for each subject was kept constant for both cycling trials.	31

List of Figures

- | | | |
|-----|---|----|
| 2.1 | The gait phase detection (dashed grey) depicted by three consecutive step cycles is computed with heel (orange) and toe (blue) ground reaction forces. The switching signal σ_p (red) determines when perturbations are applied. The ankle perturbation is not applied in the first two steps ($\sigma_p = 0$). Then, the kinematic perturbation is applied in the third step during mid-late stance phase ($\sigma_p = 1$). The phases transition between $phase = 0$ (swing), $phase = 1$ (heel strike and early stance), $phase = 2$ (perturbation region in mid-late stance), and $phase = 3$ (stop perturbation in terminal stance), which ensures the perturbation is halted prior to the start of the swing phase. The perturbation region is denoted by $\sigma_p = 1$ depicted by the shaded orange region in the third step. | 9 |
| 2.2 | Cable-driven lower-limb exoskeleton platform. The system incorporates a hybrid exoskeleton for treadmill walking using a safety harness to provide fall protection. The hybrid exoskeleton combines motors attached to Bowden cables. Encoders are installed on the ankle joint and force sensors underneath the sole of the foot to assist with gait phase detection. Real-time data is accessed through the DAC board. | 10 |
| 2.3 | The wearable orthosis is connected to a cable-driven system actuated by an electric motor to apply torque inputs about the ankle joint using the controller in (3.9). The cable applies tension as shown using the red arrow to rotate the ankle joint q . The perturbations are applied as dorsiflexions (DF) or upward rotations of the ankle. The toe and heel ground reaction forces are collected using force sensitive resistors. EMG measurements are collected on the soleus muscle. | 11 |
| 2.4 | Motorized FES-cycling testbed. The cycling system integrates an electric motor mounted on the frame to drive the chain and a portable stimulator that applies a voltage potential using surface electrodes applied on the quadriceps muscle groups. | 12 |
| 2.5 | Participants seated in the cycle wearing a garment on both thighs (not depicted here for clarity), which contains the vibration motors. The pair of FES electrodes lie below the garment and are placed in the proximal and distal part of the quadriceps muscle group on both legs. | 13 |

3.1	Block diagram of the human-robot system. The participant wears the ankle orthosis during walking. The ankle joint angle and velocity, q, \dot{q} , and the soleus muscle activity (EMG) are collected. The soleus EMG is rectified and low-pass filtered to obtain S , which is the input to the ESC algorithm. ESC computes the perturbation angle trajectory Q_d for the next perturbed step using the soleus EMG data from the previous perturbed step. The median of the trajectory Q_d is denoted as \tilde{Q}_d . Concurrently, a Bézier curve q_b is implemented to generate the deviation from the actual ankle angle trajectory q to apply the joint perturbation and then smoothly connect to the natural ankle trajectory (outside of the perturbation region). The perturbation trajectory q_d used for the tracking objective is obtained as $q_d = \tilde{Q}_d q_b$. Figure 3.2 depicts the average perturbation trajectory q_d and the ankle angle q obtained from a gait trial. The tracking controller u_e applies the perturbation input using the tracking errors e, r .	15
3.2	The average ankle joint q (blue) and desired ankle angle q_d (orange) as a function of the step cycle of all perturbed walking steps for Subject 1. The perturbation trajectory q_d deviates from q inside the shaded perturbation region as a result of the Bézier curve generation q_b and the perturbation magnitude \tilde{Q}_d . Outside of the perturbation region q_d smoothly follows q to avoid perturbing the ankle.	23
3.3	The terminal error is the ankle joint position tracking error, e_T , at the end of the controllable mid-late stance region of perturbed steps as a function of step cycles for Subject 1. The dashed red line denotes zero terminal error at the end of the perturbation region.	24
3.4	The desired, perturbation angle denoted as \tilde{Q}_d is the median of Q_d computed in (3.2) for all subjects. The evolution of the perturbation magnitudes is shown for the duration of the experiments. Perturbations with a magnitude of two degrees are first applied for the initial 60 seconds of all experiments (for familiarization) and then ESC algorithm is activated with an initial condition of 1 degree.	24
3.5	The rectified and filtered average soleus muscle response as a function of the step cycle of ESC perturbed (blue) and unperturbed (orange) walking steps for subject 1. The shaded region denotes the perturbation region.	25
4.1	Switching signal of FES and motor regions. The FES region is active when $\sigma_m = 1$ such that the quadriceps receive stimulation. The electric motor is active for all time to ensure constant cadence of 65 rpm.	28
4.2	The cadence for the duration of one trial. The electric motor assisted FES-cycling to maintain a cadence of 65 RPM.	29

- 4.3 The FES command of the left and right quadriceps stimulation patterns. FES was applied only within the kinematic efficient regions. The stimulation frequency and current amplitude of FES were fixed at 60 Hz and 80 mA, respectively. The pulse width was selected to evoked 4 N*m. The pulse width was remained constant between experiment trials. 29
- 4.4 Each data point represents the mean value of the active torque over all participants. The maximum torque for each participant was achieved at a different number of contractions. SEM stands for the standard error of the mean. 30

Acknowledgements

I would like to extend my thanks to the Nicholas Rubino, Dr. Jonathan Casas, Dr. Chen-Hao Chang, Jade Carter, and Miguel Manchola, and Steven Evangelos for developing the test beds, with the implementation of the experiments, and supporting the publications of the presented work. I would like to thank my advisor Dr. Victor Duenas for supporting the development of this thesis paper and two conference paper submissions. I would like to thank Steven Evangelos for reading the presented thesis. Finally, I would like to thank Dr. Steven Brouse and Dr. Aiko K. Thompson for their ongoing collaboration with the Bionics, Systems, and Controls (BSC) laboratory.

Chapter 1

Introduction

Powered systems that physically interact with humans need to adapt their responses to ensure stability and safety. Controllers for rehabilitation robots interacting with people with neurological impairments should ensure safe human-machine interaction and seamlessly customize the assistance for participants with different functional capacities. Thus, advancing the control algorithms of rehabilitation robotic devices can accelerate their adoption in clinical settings, thereby having the potential to make a significant impact on patients' recovery.

This chapter introduces the integration and control of a powered ankle-foot orthosis with electromyography (EMG) and motorized FES-cycling with muscle vibration as two lower-limb rehabilitation applications.

1.1. Rehabilitation with Hybrid Machines

Neurological disorders (NDs) such as spinal cord injury (SCI) and stroke result in partial or total loss of motor and sensory functions, significantly impacting an individual's independence and quality of life [1], [2]. Restoring and improving motor function is a priority for individuals with NDs, as it is crucial in enhancing their overall well-being and daily activities [1], [3]. FES-cycling is a rehabilitative strategy typically prescribed, wherein a voltage potential is applied to

lower-limb muscles to induce controlled contractions and facilitate pedaling a cycle, either with or without motorized assistance [7]. FES-cycling has been shown to impart cardiovascular and physiological benefits, thereby improving the quality of life for individuals with NDs [8]–[10]. In motorized FES-cycling, FES is applied to multiple muscle groups to evoke active torque complemented by the assistance of an electric motor [11]. FES-cycling is recommended for people with increased fall risks and impaired sensory feedback who are excluded from gait training or other high cardiovascular exercises.

Another potential approach for restoring function in people with NDs is the development of active orthotic devices, such as robotic exoskeletons, aimed at assisting gait rehabilitation [3], [12], [13]. Powered exoskeletons improve range of motion, gait function, and endurance [4], [5]. Exoskeletons enable individuals with NDs to engage in overground walking or treadmill-based walking with body weight support, which helps partially offload the user's weight and is particularly beneficial for individuals with limited weight-bearing capacity [6]. However, typical robotic-assisted approaches cannot ensure people with NDs will retain gait benefits once the assistance provided by the device is removed. A technical challenge is to integrate wearable devices and their controllers during these novel gait training strategies that promote lasting gait benefits.

1.1.1. Powered Exoskeletons for Walking with EMG

Exoskeletons can impose gait patterns that aim to replicate normal activation of muscles [14], however, the effectiveness of such approaches to induce lasting gait benefits is limited. The ankle joint and plantarflexors are critical for walking because they store mechanical energy throughout the stance phase leading to propulsive push-off [15], [16]. However, muscle activation patterns are diminished in the paretic leg after a stroke. In particular, the soleus muscle is not loaded correctly, which limits propulsion and gait speed. Targeting the soleus muscle during walking can

facilitate training and promote lasting gait benefits [17] (e.g., natural soleus activity and increased propulsion). However, stroke survivors can develop a reliance on robotic devices that can result in misuse of the paretic leg [18]. Thus, rehabilitation strategies must challenge participants without developing a dependence on the assistive devices.

While the wearability and design aspects of exoskeletons are crucial, the effectiveness of their gait patterns heavily relies on the control algorithms employed. A backstepping controller with an integral control input was developed to target the soleus muscle using surface electromyography (EMG) to track an imposed perturbation profile [19]. EMG is a data sensing tool that measures the voltage difference of the recruitment of a motor unit action potential (m.u.a.p) between two electrodes. However, it is unknown how to determine the optimal perturbation magnitude during walking to accommodate for the specific characteristics of the participants. Hence, an online adaptive strategy is well-motivated to compute the perturbation magnitude based on the muscle responses during walking.

Extremum seeking control (ESC) is an adaptive-based method that leverages an unknown input-output map with a local or global extremum to implement online optimization of a nonlinear system [20]. The classical ESC architecture uses a dither signal to inject excitation and explore the neighborhood around a setpoint to find the extremum. One of the main advantages of ESC is that knowledge of the cost function and the input-output map do not need to be known [20]. In the context of human-robot interaction, ESC has been used to control lower-limb prostheses [21], maximize the human's power output in an exercise machine [22], and with functional electrical stimulation-induced cycling [23]. This paper exploits the ESC as a real-time adaptive method to compute the ankle kinematic perturbation magnitude (i.e., joint angle deviation from the natural ankle kinematics) to characterize the unknown ankle angle-soleus muscle activation map (i.e., the relationship between the perturbation input and the muscle output).

1.1.2. Motorized FES-Cycling with Muscle Vibration

Functional electrical stimulation (FES) has been used to facilitate lower-limb movement and improve muscle mass, muscle strength, bone mineral density, and blood flow [24], [25]. FES-cycling is recommended for people with impaired sensory feedback who are excluded from gait training or other high cardiovascular exercises. Motorized FES-cycling applies electrical stimuli to activate the rider's muscles and engages an electrical motor to provide assistance as needed [26]. Motorized assistance enables repetitive practice and aids to delay the onset of muscle fatigue. However, providing more machine assistance than needed can induce passive cycling and reduce the therapeutic benefits of FES. Inevitably neuromuscular muscle fatigue settles, thus inducing a decay in the peak force generated by the muscles. Hence, motivation exists to develop strategies that increase functional recovery for prolonged periods during FES-cycling.

An outstanding challenge for the implementation of FES-powered devices is the need to achieve long-duration rehabilitation sessions to maximize physiological and cardiovascular benefits. Muscular fatigue develops more rapidly using FES than volitional contractions, limiting the overall effectiveness of FES [27], [28]. This phenomenon is due to the reverse recruitment order of motor units (i.e., opposite to the size principle) or recruitment of motor units using a nonselective, synchronous and spatially fixed pattern [29]. An additional challenge for FES-cycling in individuals with NDs is the physical interference associated with spasticity characterized by muscle spasms and pain. Involuntary muscle spasms limit the duration, intensity and dosage of active cycling. Hence, despite the benefits of FES-cycling, muscle fatigue and physical disturbances resulting from spasms and pain interfere with cycling and degrade the functional benefits. There is a need to improve hybrid rehabilitation strategies to cope with these challenges and enable a wider adoption of FES-cycling at home and the community.

Mechanical vibration or vibratory stimuli have been implemented to provide sensory feedback in application to alleviate chronic pain [30], increase muscle power [31], induce muscular ac-

tivity, improve lower limb kinematics, and enhance conventional resistance exercise gains [32], [33]. Customized motor-vibration systems have been designed for whole-body vibration (WBV) platforms [34]. Moreover, hand-held vibration devices are used to manually apply the vibration over muscles. WBV and local vibration have reduced spasticity and increased muscle activity attributed to reflex activity modulation [35], [36]. The vibration frequencies in [35], [36] range from low frequencies 20-50 Hz for WBV to high frequencies 300-500 Hz using local vibration devices. Vibration has increased muscle activity, reduced sway while standing, and induced muscle forces when applied to the Achilles tendon [37]. The increase in muscle activity due to vibration has been explained through muscle spindle-induced reflexive recruitment of inactive motor units [34], [38]. The modulation of afferent inputs achieved through tendon and muscle vibration is known to be a strong stimulus for the activation of muscle spindle primary endings, thereby stimulating sensory and motor cortical areas [38]. However, it is unknown whether vibratory stimuli applied during FES-cycling can influence the force generated by muscles and delay the onset of muscle fatigue.

Vibration stimuli applied to the tendon or muscle belly has been suggested to induce motor activation and modulate afferent inputs [39], [40]. Moreover, vibration targeting tendons has shown to attenuate spastic-like activity, which may aid to mitigate involuntary muscle spasms in people with SCI [41]. Vibration applied to the muscle belly of the quadriceps, hamstrings, and tensor fascia latae muscles has elicited step-like responses in individuals with SCI [41]. Prolonged vibrational stimuli over the rectus femoris for 10 minutes shows significant reduction in leg spasticity after SCI [42]. In a recent study, constant superimposition tendon vibration had no effects on wide-pulse low frequency neuromuscular electrical stimulation (NMES) applied on the quadriceps during plantar flexion motion [43]. It was suggested that NMES induced saturation of the Ia afferents and, thus, the muscle was over activated. It has been also suggested that vibration may be more effective if it is brief or intense to produce a synchronous afferent flow [33]. Thus, motivation exists to examine intermittent strategies to modulate the vibration timing and magnitude and assess the impact of mechanical vibration in the muscle active torque output during

electrically elicited contractions.

Combining vibratory and electrical stimuli may provide neural adaptations and enhanced muscle performance, optimized by stimulation of sensory axons. Even though the present work also investigated coupling mechanical vibration and electrical stimulation, there are differences compared to the study in [44]. In [44] the Achilles tendon was vibrated providing an afferent input. Finally, in [44] the authors may have been able to trigger a centrally mediated excitatory mechanism (in addition to the peripheral sensory activation) by applying vibration to the Achilles tendon.

The motivation of the present study is to examine the influence of vibratory stimuli for adapting the muscle capacity to evoke active torque during cycle, given that previous studies have shown isometric torque increments during electrical stimulation coupled with vibratory stimuli. In [44], increased extra torques (generated by vibratory stimuli) were found to reach values up to 50% of the maximum voluntary contractions on top of the peripheral torque elicited by percutaneous electrical stimulation. Vibratory stimuli of 100 Hz for 2-second periods were applied to the Achilles tendon while alternating with electrical stimulation. However, some subjects exhibited no extra force produced by vibration. Hence, motivation exists to uncover the potential effects of the combination of vibration and FES during cycling.

Chapter 2

Dynamic Models and Experimental Setup

In this chapter, the nonlinear dynamic model is presented for the ankle orthosis system. Experimental test beds for the ankle-foot orthosis and cycling systems are described.

2.1. Powered Ankle-Foot Orthosis System

The single degree-of-freedom ankle-joint muscle-tendon and powered orthosis system can be modeled as a phase-dependent switched system with the following Euler-Lagrange dynamics

$$J\ddot{q}(t) + f(q(t), \dot{q}(t)) + G(q(t)) + d(t) = \tau(t), \quad (2.1)$$

where $J \in \mathbb{R}_{>0}$ is an uncertain positive constant denoting the combined inertia of the overall ankle-foot orthosis and joint-muscle system; $\ddot{q} : \mathbb{R}_{\geq t_0} \rightarrow \mathbb{R}$ denotes the unmeasurable ankle angular acceleration; the nonlinear function $f : \mathcal{Q} \times \mathbb{R} \rightarrow \mathbb{R}$ denotes the elasticity due to the ankle stiffness and the viscous effects due to damping in the musculotendon complex as derived in [45], [46]; $G : \mathcal{Q} \rightarrow \mathbb{R}$ denotes the effects of gravity; and $d : \mathbb{R}_{\geq t_0} \rightarrow \mathbb{R}$ denotes the external disturbances. The torque applied by the electric motor about the ankle joint is denoted by $\tau : \mathbb{R}_{\geq t_0} \rightarrow \mathbb{R}$ and is defined as

$$\tau(t) \triangleq \sigma_p B_e u_e(t), \quad (2.2)$$

where $u_e : \mathbb{R}_{\geq t_0} \rightarrow \mathbb{R}$ is the motor current control input designed subsequently, $B_e \in \mathbb{R}_{>0}$ is a known positive torque constant, and $\sigma_p \in \{0, 1\}$ is a piecewise constant switching signal developed to apply an ankle joint perturbation per step cycle within the mid-late stance phase of walking (i.e., the perturbation region). The switching signal is defined as $\sigma_p = 1$ within the perturbation region and $\sigma_p = 0$ outside of the perturbation region to stop perturbing the ankle joint and thus, interfering with natural ankle kinematics. A gait phase detection algorithm is implemented to compute the switching signal σ_p using heel and toe ground reaction forces to determine the heel strike and define the perturbation phase. The phases transition between $phase = 0$ (swing), $phase = 1$ (heel strike and early stance), $phase = 2$ (perturbation region in mid-late stance), and $phase = 3$ (stop perturbation in terminal stance), which ensures the perturbation is halted prior to the start of the swing phase. The perturbation region is denoted by $\sigma_p = 1$ depicted by the shaded orange region in the third step. The ankle angular velocity \dot{q} is used to determine when to stop the perturbation phase. The perturbation phase ends when the ankle joint reaches peak dorsiflexion such that \dot{q} becomes $\dot{q} > 0$. Figure 2.1 depicts the transition of gait phases, the toe and heel forces and an example of a perturbation region (i.e., the shaded region when $\sigma_p = 1$).

The following assumption and properties are exploited the subsequent control design and analysis.

Assumption 1. *The additive disturbance d is bounded as $|d| \leq \zeta_d$, where $\zeta_d \in \mathbb{R}_{>0}$ is a known positive constant.*

Property 1. $|f(q, \dot{q})| \leq c_{f1} + c_{f2}|\dot{q}|$, where $c_{f1}, c_{f2} \in \mathbb{R}_{>0}$ are known constants.

Property 2. $|G(q)| \leq \bar{g}$, where $\bar{g} \in \mathbb{R}_{>0}$ is a known constant [47, Ch. 3].

The exoskeleton is shown in Figure 2.2. Participants wear a safety harness connected to a portable track for fall protection. The apparatus consists of a powered, wearable ankle-foot orthosis that is customizable to various foot sizes. Figure 2.3 depicts the wearable ankle device. Straps are utilized around the foot and shank to maintain alignment with the user's ankle joint. The wear-

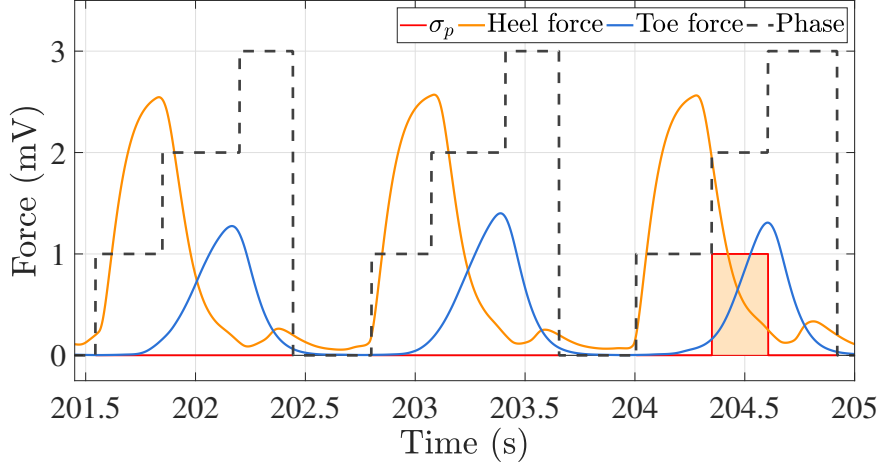


Figure 2.1: The gait phase detection (dashed grey) depicted by three consecutive step cycles is computed with heel (orange) and toe (blue) ground reaction forces. The switching signal σ_p (red) determines when perturbations are applied. The ankle perturbation is not applied in the first two steps ($\sigma_p = 0$). Then, the kinematic perturbation is applied in the third step during mid-late stance phase ($\sigma_p = 1$). The phases transition between $phase = 0$ (swing), $phase = 1$ (heel strike and early stance), $phase = 2$ (perturbation region in mid-late stance), and $phase = 3$ (stop perturbation in terminal stance), which ensures the perturbation is halted prior to the start of the swing phase. The perturbation region is denoted by $\sigma_p = 1$ depicted by the shaded orange region in the third step.

able orthosis has a mechanism to apply joint perturbations using cable-driven actuation as in [48], [49]. The device is connected to a separate actuation unit with a brushless 24 VDC electric motor (Maxon International Ltd.) to apply torque inputs about the ankle joint. An optical encoder (US Digital) is mounted on the orthosis to measure the ankle joint angular position q and velocity \dot{q} . The heel and toe reaction forces are measured using force sensitive resistors (FlexiForceA401), which are placed within the sole of the foot orthosis. EMG data of the soleus muscle is collected using two 0.875×1.375 inch electrode pads (13-NEURO PLUS A10041-60) placed one inch apart along the center line of the lower leg below the head of the gastrocnemius. The surface electrodes are connected to a Bortec AMT-8 amplifier to amplify and send the EMG data to the data acquisition board (QPIDE, Quanser). The controller is implemented on a desktop computer (Windows 10 OS) running a real-time target (QUARC 2.6, Quanser) using MATLAB/Simulink 2018a (Mathworks, Inc). A modified treadmill (NordicTrack T7.5S) is used for the walking experiments and a closed-loop controller is implemented to keep the treadmill belt at the desired constant

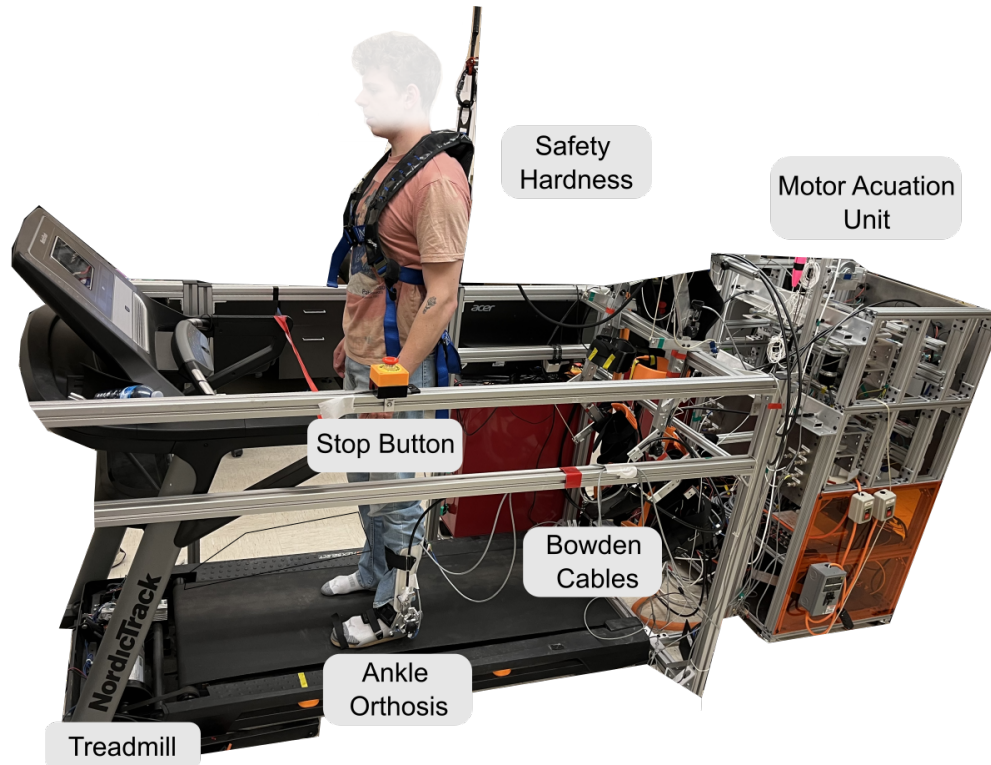


Figure 2.2: Cable-driven lower-limb exoskeleton platform. The system incorporates a hybrid exoskeleton for treadmill walking using a safety harness to provide fall protection. The hybrid exoskeleton combines motors attached to Bowden cables. Encoders are installed on the ankle joint and force sensors underneath the sole of the foot to assist with gait phase detection. Real-time data is accessed through the DAC board.

walking speed. For safety purposes, the participants have access to an emergency stop button and software stop conditions are implemented to limit the amount of motor current compliant with hardware limits. The measured EMG response is rectified and passed through a low-pass filter with a 25 rad/sec cutoff frequency.

2.2. Motorized FES-Cycling

Cycling experiments are performed using a recumbent cycle (Sun Seeker ECO-TAD SX) mounted on an indoor trainer, adapted with orthotic boots, and equipped with a 24 VDC brushed electric motor. A torque transducer (SRM, Germany) was utilized to measure the cycle crank torque. An

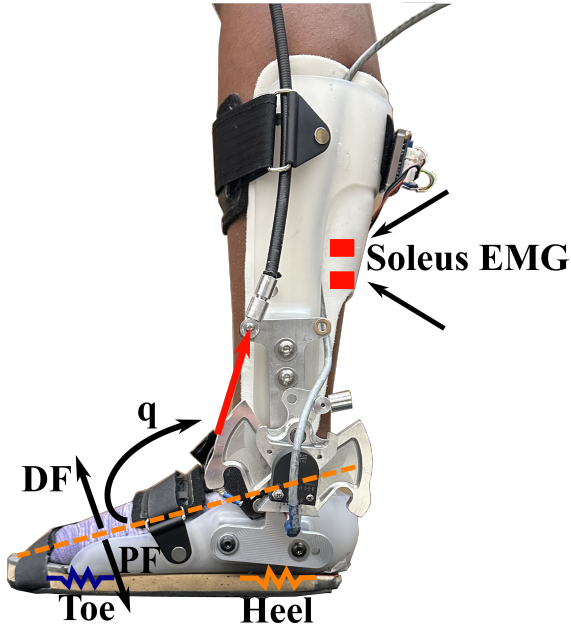


Figure 2.3: The wearable orthosis is connected to a cable-driven system actuated by an electric motor to apply torque inputs about the ankle joint using the controller in (3.9). The cable applies tension as shown using the red arrow to rotate the ankle joint q . The perturbations are applied as dorsiflexions (DF) or upward rotations of the ankle. The toe and heel ground reaction forces are collected using force sensitive resistors. EMG measurements are collected on the soleus muscle.

optical encoder (US Digital) was coupled to the cycle crank to measure the crank position. A data acquisition device (Quanser QPIDe, Quanser, Canada) was used with a personal computer executing MATLAB/Simulink 2018a (MathWorks Inc) for data logging with a sampling rate of 1 kHz. An analog motor driver (Advanced Motion Controls) commanded the current control to the electric motor. Biphasic symmetric rectangular stimulation pulses were delivered by a current controlled electrical stimulator (RehaStim, Hasomed GmbH, Germany). A single stimulation channel was used with a pair of 3" by 5" bipolar self-adhesive surface electrodes placed over the distal-medial and proximal-lateral portions of the quadriceps muscle group on both legs [surface electrodes for the study were provided compliments of Axelgaard Manufacturing Co., Ltd. (ValuTrode®, USA)]. The mechanical stimulus was applied to the quadriceps muscle belly using vibratory motors of 9 mm diameter (Pico VibeTM, Precision Microdrives, United Kingdom) affixed to the leg using an adjustable garment. Each vibratory motor was controlled by applying a 3V voltage command to achieve a frequency of 230 Hz, which was perceptible, and a vibration



Figure 2.4: Motorized FES-cycling testbed. The cycling system integrates an electric motor mounted on the frame to drive the chain and a portable stimulator that applies a voltage potential using surface electrodes applied on the quadriceps muscle groups.

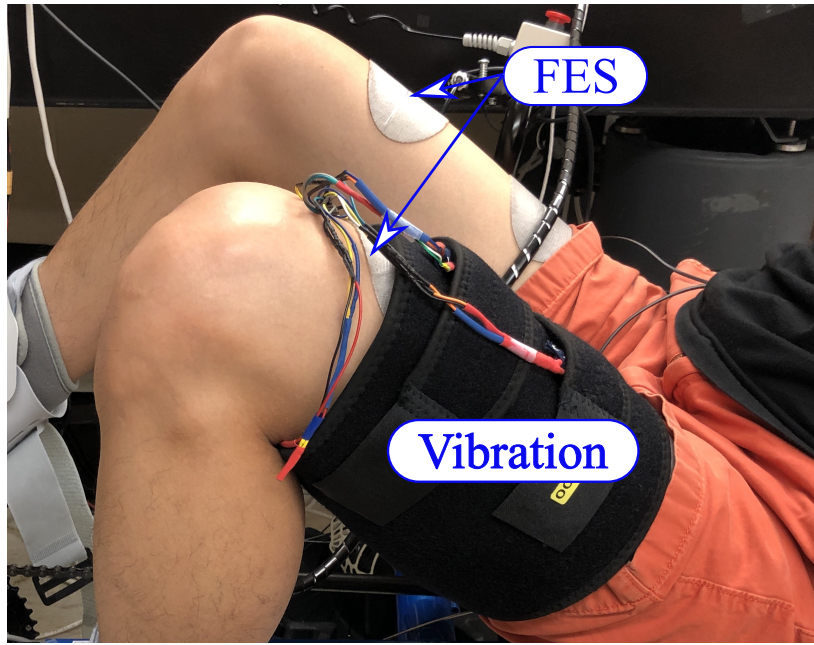


Figure 2.5: Participants seated in the cycle wearing a garment on both thighs (not depicted here for clarity), which contains the vibration motors. The pair of FES electrodes lie below the garment and are placed in the proximal and distal part of the quadriceps muscle group on both legs.

amplitude of 7g (g-force or acceleration of gravity). Six vibration motors were used to apply the vibratory stimuli bilaterally. The garments were secured to the participant's thighs using Velcro straps to provide an appropriate fit and ensure direct contact between the vibration motors and the muscle belly. The placement of the garment with the vibration motors and FES electrodes is depicted in Figure 2.5.

Chapter 3

Extremum Seeking Control Targeting the Soleus Muscle During Walking

In this Chapter, an ESC algorithm leveraging the architecture in [20], [22], [50] is developed to compute the ankle perturbation angle using a motorized ankle-foot orthosis and soleus EMG measurements. The objective is to perturb the ankle joint using the device to generate increments in soleus muscle responses (i.e., maximize the muscle activity) during walking. The capacity to modulate the soleus muscle responses using the device despite differences across participants (e.g., differences in muscle force production, joint kinematics, etc.) will be exploited in subsequent studies for gait training. A closed-loop robust feedback controller is designed to track the computed perturbation by the ESC algorithm during the mid-late stance phase of walking. A piecewise continuous switching signal is developed to activate the perturbation controller using ground reaction force measurements and the ankle angle velocity to stop the perturbation. A Lyapunov-based stability analysis is developed to ensure global exponential tracking of the perturbation trajectory. Treadmill walking experiments in four healthy young adults were conducted for validation of the developed control methods.

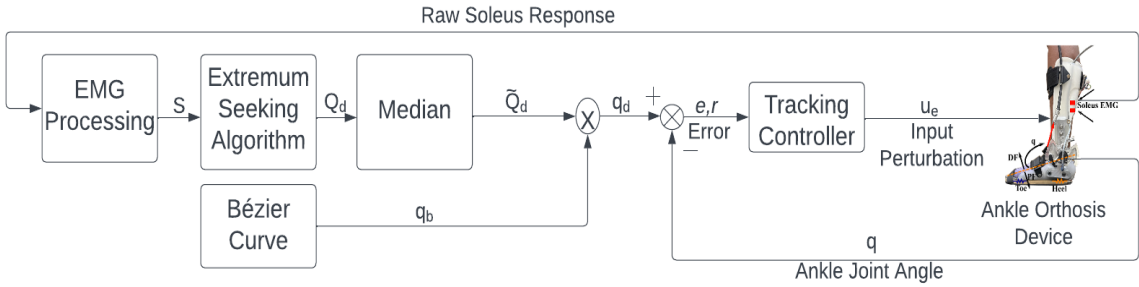


Figure 3.1: Block diagram of the human-robot system. The participant wears the ankle orthosis during walking. The ankle joint angle and velocity, q , \dot{q} , and the soleus muscle activity (EMG) are collected. The soleus EMG is rectified and low-pass filtered to obtain S , which is the input to the ESC algorithm. ESC computes the perturbation angle trajectory Q_d for the next perturbed step using the soleus EMG data from the previous perturbed step. The median of the trajectory Q_d is denoted as \tilde{Q}_d . Concurrently, a Bézier curve q_b is implemented to generate the deviation from the actual ankle angle trajectory q to apply the joint perturbation and then smoothly connect to the natural ankle trajectory (outside of the perturbation region). The perturbation trajectory q_d used for the tracking objective is obtained as $q_d = \tilde{Q}_d q_b$. Figure 3.2 depicts the average perturbation trajectory q_d and the ankle angle q obtained from a gait trial. The tracking controller u_e applies the perturbation input using the tracking errors e, r .

3.1. Control Development

Figure 3.1 depicts the block diagram of the closed-loop ankle perturbation controller. The participant wears a robotic ankle-foot orthosis during walking. The soleus muscle activity (denoted S after signal processing) and ankle angular position and velocity q , \dot{q} are measurable. An ESC algorithm is implemented to generate the ankle perturbation trajectory and a nonlinear robust controller is designed to track the perturbation, and thus, apply the perturbation about the ankle joint using the device. The ESC algorithm and robust tracking controller are developed in the following subsections.

3.1.1. Extremum Seeking Control for Ankle Perturbation Trajectory Generation

To apply perturbations about the ankle joint, a kinematic perturbation trajectory $q_d : \mathbb{R}_{\geq t_0} \rightarrow \mathbb{R}$ can be generated using ESC such that $q_d \in \mathcal{L}_\infty$ and $q_d \rightarrow q_d^*$, where q_d^* is an unknown optimal perturbation magnitude that maximizes the participant's soleus muscle response during walking (i.e., generate the largest increment in muscle response). The perturbation trajectory is obtained by imposing a deviation from the natural ankle kinematics within the mid-late stance phase of walking. A Bézier curve $q_b : \mathbb{R}_{\geq t_0} \rightarrow \mathbb{R}$ is designed to depart from the current natural ankle joint trajectory q (i.e., the actual ankle position), impose the perturbation (i.e., an ankle dorsiflexion), and then connect back to the natural ankle trajectory in real-time. However, the perturbation magnitude $\tilde{Q}_d \in \mathbb{R}_{>0}$ (i.e., the peak dorsiflexion) that yields predictable soleus muscle activity increments is unknown. Hence, the ESC algorithm computes a perturbation magnitude trajectory $Q_d : \mathbb{R}_{\geq t_0} \rightarrow \mathbb{R}$ that is used to calculate \tilde{Q}_d . The ESC algorithm and the Bézier curve are then used to generate the perturbation trajectory $q_d(t)$ for the control tracking objective as illustrated in the block diagram in Figure 3.1.

The measurable soleus muscle response $S : \mathcal{Q} \times \mathbb{R} \times \mathbb{R}_{\geq t_0} \rightarrow \mathbb{R}_{\geq t_0}$ can be modeled as [51], [52]

$$S(q, \dot{q}, t) = s_1 + s_2 q(t) + s_3 \dot{q}(t), \quad (3.1)$$

which is measurable using EMG, $q : \mathbb{R}_{\geq t_0} \rightarrow \mathcal{Q}$ denotes the measurable ankle joint angular position, $\dot{q} : \mathbb{R}_{\geq t_0} \rightarrow \mathbb{R}$ denotes the measurable angular velocity, $\mathcal{Q} \subseteq \mathbb{R}$ is the set of ankle angles, $t_0 \in \mathbb{R}$ is the initial time, and $s_1, s_2, s_3 \in \mathbb{R}_{>0}$ are uncertain positive constants. The objective of the ESC algorithm is to yield increments of the steady state value of soleus muscle response S due to the applied ankle perturbations without requiring the knowledge of q_d^* . The only assumption is that q_d^* exists such that each participant can evoke a maximum soleus response

during walking. Inspired by ESC algorithms [22], [23], [50] that leverage dither signals to aid with convergence to a neighborhood of the extremum, a saturated extremum-seeking algorithm is developed to generate the ankle dorsiflexion (perturbation) magnitude profile $Q_d : \mathbb{R}_{\geq t_0} \rightarrow \mathbb{R}$ as

$$\begin{aligned} w &= -(k_h^2 \nu + k_h \text{sat}_\beta(S)), \\ \dot{\hat{\theta}} &= -k_\theta w \sin(\omega q), \\ \dot{\nu} &= -(k_h \nu + \text{sat}_\beta(S)), \\ Q_d &= \hat{\theta} + (\alpha_p - \frac{k_d}{\alpha_p} w) \sin(\omega q), \end{aligned} \tag{3.2}$$

which leverages S from the previous perturbed step to generate the perturbation trajectory for the next perturbed step computed as $q_d(t) \triangleq \tilde{Q}_d q_b(t)$, where $\tilde{Q}_d \triangleq \text{med}(Q_d)$ is the median of Q_d . In the ESC algorithm in (3.2), $\alpha_p \in \mathbb{R}_{>0}$ denotes a positive constant amplitude of the dither signal, $\omega \in \mathbb{R}_{>0}$ denotes the frequency of the dither, $k_d, k_\theta, k_h \in \mathbb{R}_{>0}$ denote positive constant parameters, $\hat{\theta}, \nu, w : \mathbb{R}_{\geq t_0} \rightarrow \mathbb{R}$ denote auxiliary signals, and $\text{sat}_\beta(\cdot)$ denotes the saturation function defined as

$$\text{sat}_\beta(\cdot) \triangleq \begin{cases} \cdot & \text{for } |\cdot| \leq \beta \\ \text{sgn}(\cdot)\beta & \text{for } |\cdot| > \beta \end{cases}, \tag{3.3}$$

where $\beta \in \mathbb{R}$ is a saturation limit and $\text{sgn}(\cdot) : \mathbb{R} \rightarrow [-1, 1]$ is the signum function. The saturation function is integrated in the ESC algorithm in (3.2) to ensure Q_d is bounded, and hence, q_d is bounded since the Bézier curve q_b is bounded by design. The ESC algorithm in (3.2) replaces the typical time-based dither signal in classical ESC with a time-invariant dither (i.e., state dependent) as in [53] to adapt the joint perturbation trajectory using the ankle angle q within the perturbation region in the stance phase of walking.

3.1.2. Ankle Perturbation Tracking Controller

To quantify the kinematic tracking objective, a measurable angular joint position error $e : \mathbb{R}_{\geq t_0} \rightarrow \mathbb{R}$ and an auxiliary filtered tracking error $r : \mathbb{R}_{\geq t_0} \rightarrow \mathbb{R}$ are defined as

$$e(t) = q_d(t) - q(t), \quad (3.4)$$

$$r(t) = \dot{e}(t) + \alpha e(t), \quad (3.5)$$

where $\alpha \in \mathbb{R}_{>0}$ is a selectable constant control gain and $q_d : \mathbb{R}_{\geq t_0} \rightarrow \mathbb{R}$ is the bounded ankle perturbation trajectory.

The open-loop error system is obtained by taking the time derivative of (3.5), pre-multiplying it by J , substituting for (2.1), (3.4) and (3.5), and performing algebraic manipulation as

$$J\dot{r} = J\ddot{q}_d + f(q, \dot{q}) + G(q) + d - \tau + J\alpha r - J\alpha^2 e. \quad (3.6)$$

Segregating terms that can be upper bounded by a positive constant and a state-dependent function, respectively, the following auxiliary signals $N_d : \mathbb{R}_{\geq t_0} \rightarrow \mathbb{R}$ and $\tilde{N} : \mathbb{R}_{\geq t_0} \rightarrow \mathbb{R}$ are defined as

$$N_d \triangleq d + J\ddot{q}_d + f(q_d, \dot{q}_d) + G(q_d), \quad (3.7)$$

$$\tilde{N} \triangleq f(q, \dot{q}) - f(q_d, \dot{q}_d) + G(q) - G(q_d) + J\alpha r - J\alpha^2 e + e, \quad (3.8)$$

where the desired dynamics $\tau_d(q_d, \dot{q}_d) : \mathbb{R}_{\geq t_0} \rightarrow \mathbb{R} \triangleq f(q_d, \dot{q}_d) + G(q_d)$ were added and subtracted in (3.7) and (3.8), respectively, to generate an upperbound of (3.8) using the mean value theorem. The auxiliary signal in (3.7) can be upper bounded as $|N_d| \leq \xi_d$ leveraging Assumption 1 and the fact that $\tau_d \in \mathcal{L}_\infty$, where $\xi_d \in \mathbb{R}_{>0}$ is a known positive constant. The auxiliary signal in (3.8) can be upperbounded as $|\tilde{N}| \leq \varrho(||z||)||z||$, where $z : \mathbb{R}_{\geq t_0} \rightarrow \mathbb{R}^2$ is defined as $z \triangleq [e \ r]^T$, and $\varrho : \mathbb{R} \rightarrow \mathbb{R}$ is a known positive, non-decreasing, radially unbounded function.

Given the open-loop error system in (3.6), the control input is designed as:

$$u_e \triangleq k_1 r + k_2 \text{sgn}(r) + k_3 \varrho^2(\|z\|)r, \quad (3.9)$$

where $k_1, k_2, k_3 \in \mathbb{R}_{>0}$ are selectable positive gain constants. The motor control input in (3.9) includes a feedback term, a high-frequency term to compensate for the auxiliary term in (3.7) that is upper bounded by a constant, and a nonlinear damping term to compensate for the auxiliary signal in (3.8) that is upper bounded by a state-dependent function. The closed-loop kinematic error system is obtained by substituting (2.2), (3.7), (3.8), and (3.9) when $\sigma_p = 1$ into (3.6) as

$$J\dot{r} = \tilde{N} + N_d - e - B_e \left(k_1 r + k_2 \text{sgn}(r) + k_3 \varrho^2(\|z\|)r \right). \quad (3.10)$$

3.2. Stability Analysis

The stability of the closed-loop ankle kinematic controller to impose joint perturbations during the mid-late stance phase can be examined using the following theorem.

Theorem 1. *The controller in (3.9) ensures global exponential joint kinematic tracking within the perturbation region, i.e., for $\sigma_p = 1$, in the sense that*

$$\|z(t)\| \leq \sqrt{\frac{\lambda_2}{\lambda_1}} \|z(t_0)\| e^{-\frac{\delta}{4\lambda_2}(t-t_0)}, \quad (3.11)$$

provided the following sufficient gain conditions are satisfied

$$k_2 \geq \frac{\xi_d}{B_e}, \quad \delta \triangleq \min\{\alpha, k_1 B_e\} > \frac{1}{2k_3 B_e}. \quad (3.12)$$

Proof. Let $V : \mathbb{R}^2 \times \mathbb{R}_{\geq t_0} \rightarrow \mathbb{R}$ be a positive definite, radially unbounded, continuously differen-

tiable Lyapunov function candidate defined as

$$V \triangleq \frac{1}{2}e^2 + \frac{1}{2}Jr^2. \quad (3.13)$$

The function in (3.13) satisfies the following inequalities

$$\lambda_1\|z\|^2 \leq V(z, t) \leq \lambda_2\|z\|^2, \quad (3.14)$$

where $\lambda_1 \triangleq \min(\frac{1}{2}, \underline{J})$ and $\lambda_2 \triangleq \max(\frac{1}{2}, \bar{J})$, where $\underline{J}, \bar{J} \in \mathbb{R}_{>0}$ are positive constant bounds of the system's inertia J . Let $z(t)$ be a Filippov solution to the differential inclusion $\dot{z} \in K[h](z)$, where $K[h](\cdot)$ is defined as in [54], and h is defined by using (3.5) and (3.10) as $h \triangleq [h_1 \ h_2]$, where

$$\begin{aligned} h_1 &\triangleq r - \alpha e, \\ h_2 &\triangleq \frac{1}{J}\{\tilde{N} + N_d - e - B_e(k_1r + k_2\text{sgn}(r) + k_3\varrho^2(\|z\|)r)\}. \end{aligned}$$

The control input in (3.9) has the signum function; hence, the time derivative of (3.13) exists almost everywhere (a.e.), i.e., for almost all t . Based on [55, Lemma 2], $\dot{V}(z, t) \stackrel{a.e.}{\in} \dot{\tilde{V}}(z, t)$, where $\dot{\tilde{V}}$ is the generalized time derivative of (3.13) along the Filippov trajectories of $\dot{z} = h(z)$ and is defined in [55] as $\dot{\tilde{V}} \triangleq \bigcap_{\xi \in \partial V} \xi^T K \begin{bmatrix} \dot{e} & \dot{r} & 1 \end{bmatrix}^T (e, r, t)$, where $\partial V(z, t)$ is the generalized gradient of V at (z, t) . Since $V(z, t)$ is continuously differentiable in z , $\partial V = \{\nabla V\}$, $\dot{\tilde{V}} \stackrel{a.e.}{\subset} [e, Jr]K \begin{bmatrix} \dot{e} & \dot{r} \end{bmatrix}^T$. Therefore, after substituting (3.5) and (3.10), canceling common terms, the generalized time derivative of (3.13) can be expressed as

$$\dot{\tilde{V}} \stackrel{a.e.}{\subset} -\alpha e^2 + r(\tilde{N} + N_d - B_e(k_1r + k_2K[\text{sgn}(r)] + k_3\varrho^2(\|z\|)r)), \quad (3.15)$$

where $K[\text{sgn}(r)] = SGN(r)$ such that $SGN(r) = 1$ if $r > 0$, $[-1, 1]$ if $r = 0$, and -1 if $r < 0$.

Substituting the upper bounds of (3.7) and (3.8), the previous expression can be upperbounded as

$$\dot{\tilde{V}} \stackrel{a.e.}{\leq} -\alpha e^2 - k_1 B_e r^2 - (k_2 B_e - \xi_d)|r| + \varrho(\|z\|)\|z\||r| - k_3 B_e \varrho^2(\|z\|)r^2. \quad (3.16)$$

By completing the squares for the last two terms in the previous inequality, (3.16) can be rewritten as

$$\dot{\tilde{V}} \stackrel{a.e.}{\leq} -\alpha e^2 - k_1 B_e r^2 - (k_2 B_e - \xi_d)|r| + \frac{1}{4k_3 B_e} \|z\|^2. \quad (3.17)$$

Provided the gain conditions in (3.12) are satisfied, the inequality in (3.17) can be further upper bounded as

$$\dot{\tilde{V}} \stackrel{a.e.}{\leq} -\frac{\delta}{2} \|z\|^2 - \left(\frac{\delta}{2} - \frac{1}{4k_3 B_e} \right) \|z\|^2. \quad (3.18)$$

By invoking [55, Corollary 2], $|e|, |r| \rightarrow 0$ as $t \rightarrow \infty$. Using the inequalities in (3.14) and (3.18) and solving the differential inequality yields (3.11). Since $\dot{V} > 0$ and $\dot{V} \stackrel{a.e.}{\leq} 0$, $V \in \mathcal{L}_\infty$; hence, $e, r \in \mathcal{L}_\infty$, which implies that $z \in \mathcal{L}_\infty$, and thus $u_e \in \mathcal{L}_\infty$ in (3.9) and $\tau \in \mathcal{L}_\infty$ in (2.2). Since $e, r \in \mathcal{L}_\infty$, then $\dot{e} \in \mathcal{L}_\infty$ from (3.5), and hence $q, \dot{q} \in \mathcal{L}_\infty$, which implies $\ddot{q} \in \mathcal{L}_\infty$ from (3.10). ■

3.3. Gait Protocol

The nonlinear closed-loop controller in (3.9) and ESC algorithm in (3.2) were implemented during treadmill walking experiments in four able-bodied participants. Prior to participation, written informed consent was obtained from the participants, as approved by the Institutional Review Board at Syracuse University. First, a three-minute pre-trial walking experiment was conducted to collect the natural ankle joint kinematics and toe and heel ground reaction forces. Then a six-minute walking experiment was conducted starting with one-minute with fixed ankle joint perturbations of a constant magnitude of two degrees to acclimate the participants to perturbations and collect soleus muscle activity to initialize the ESC algorithm. After one minute, the

ESC algorithm started to adapt the perturbation magnitude for five additional minutes.

Perturbations were applied every three steps such that the participant had resumed normal gait walking after two unperturbed steps (i.e., to prevent habituation to the perturbations). A metronome was used to promote consistent cadence (steps per second) and thus, obtain quasi-cyclical ankle joint trajectories q to ensure steady walking for improving performance of the ESC algorithm. The participant was instructed to follow the metronome to ensure a constant cadence and sufficient time was allowed for familiarization before applying the perturbations. During all walking experiments the participants walked on a treadmill at a comfortable, moderate speed of 1.0 m/s.

3.4. Results

The tracking control gains introduced in (3.5) and (3.9) were selected as $\alpha \triangleq 4$, $k_1 \in [0.026, 0.070]$, $k_2 \in [0.18, 0.63]$, $k_3 \in [1.3 * 10^{-7}, 3.5 * 10^{-5}]$ during all the experiments. The ESC parameters in (3.2) were selected as $\alpha_p \triangleq 0.25$, $k_h \in [19, 20]$, $k_\theta \triangleq 40$, $k_d \in [0.1, 0.3]$, $\omega \triangleq 4$.

The average ankle joint angle and perturbation trajectory are depicted in Figure 3.2 as a function of the step cycle for Subject 1. To quantify the tracking performance of the perturbation objective the terminal error e_T is calculated. The terminal error e_T is defined as the error in (3.4) at the point of peak dorsiflexion in the end of the perturbation region. The average terminal error across all participants remained at $\bar{e}_T = 14.36 \pm 12.23\%$ suggesting bounded and suitable kinematic tracking as illustrated in Figure 3.3 for Subject 1.

The ESC algorithm computed the ankle perturbation angle for the next perturbed step exploiting the processed EMG of the soleus muscle in the previous perturbed step. Figure 3.4 depicts the computed perturbation angles for the four participants demonstrating the capacity of the ESC to personalize the ankle perturbation and remain bounded.

Table 3.1: The average terminal error, \bar{e}_T , average desired angle, \bar{Q}_d , and the percent error $\%e_T$ that represents the ratio of the terminal error to desired perturbation angle $\frac{\bar{e}_T}{\bar{Q}_d}$. The average soleus muscle EMG activity \bar{S} is reported for the first 10 and last 10 perturbed steps with ESC.

	Avg. Terminal Error \bar{e}_T (deg)	Avg. Desired Angle \bar{Q}_d (deg)	Percent Terminal Error $\%e_T$	First 10 Steps	Last 10 Steps
Subject 1	0.52 ± 0.66	5.40 ± 1.07	9.98 ± 12.68	0.0816 ± 0.0089	0.0878 ± 0.0070
Subject 2	0.89 ± 0.52	6.37 ± 1.19	13.95 ± 8.19	0.0670 ± 0.0056	0.0672 ± 0.0101
Subject 3	1.82 ± 1.08	8.37 ± 2.50	20.92 ± 12.60	0.0684 ± 0.0012	0.0695 ± 0.0095
Subject 4	0.50 ± 0.61	4.09 ± 0.55	12.59 ± 15.47	0.0161 ± 0.0012	0.0091 ± 0.0011
Mean (S1-S4)	0.93	6.06	14.36	0.0582	0.0584
STD*(S1-S4)	0.71	1.83	12.23	0.0042	0.0069

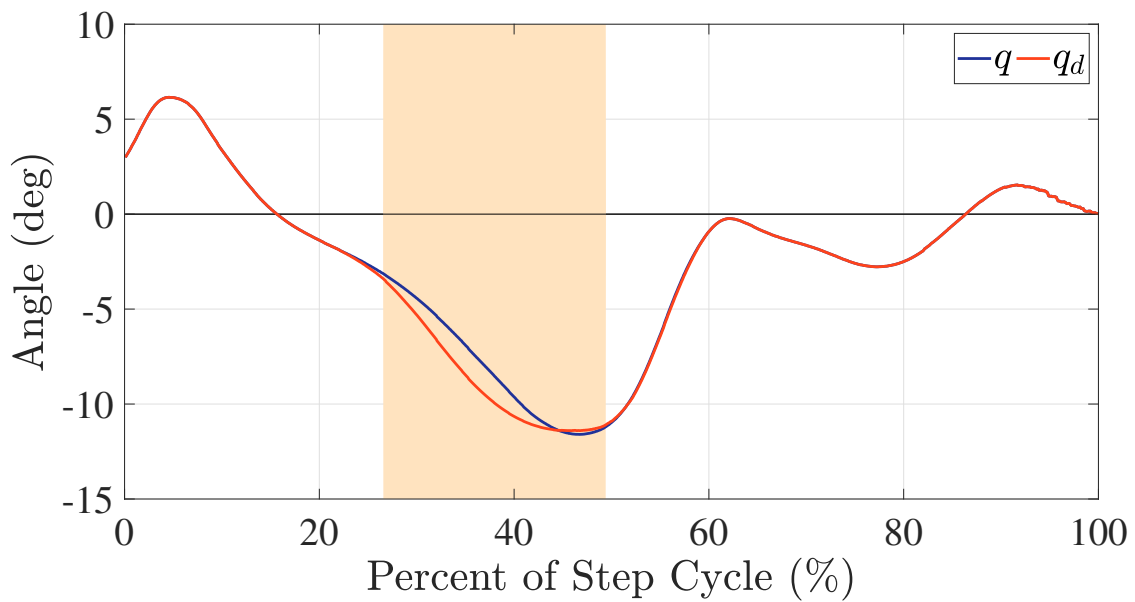


Figure 3.2: The average ankle joint q (blue) and desired ankle angle q_d (orange) as a function of the step cycle of all perturbed walking steps for Subject 1. The perturbation trajectory q_d deviates from q inside the shaded perturbation region as a result of the Bézier curve generation q_b and the perturbation magnitude \tilde{Q}_d . Outside of the perturbation region q_d smoothly follows q to avoid perturbing the ankle.

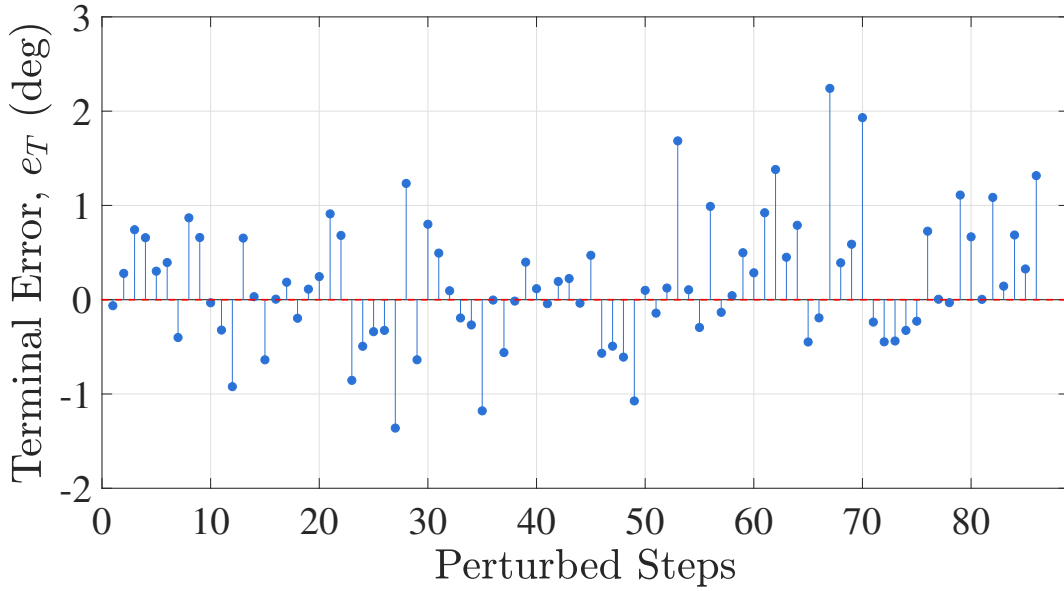


Figure 3.3: The terminal error is the ankle joint position tracking error, e_T , at the end of the controllable mid-late stance region of perturbed steps as a function of step cycles for Subject 1. The dashed red line denotes zero terminal error at the end of the perturbation region.

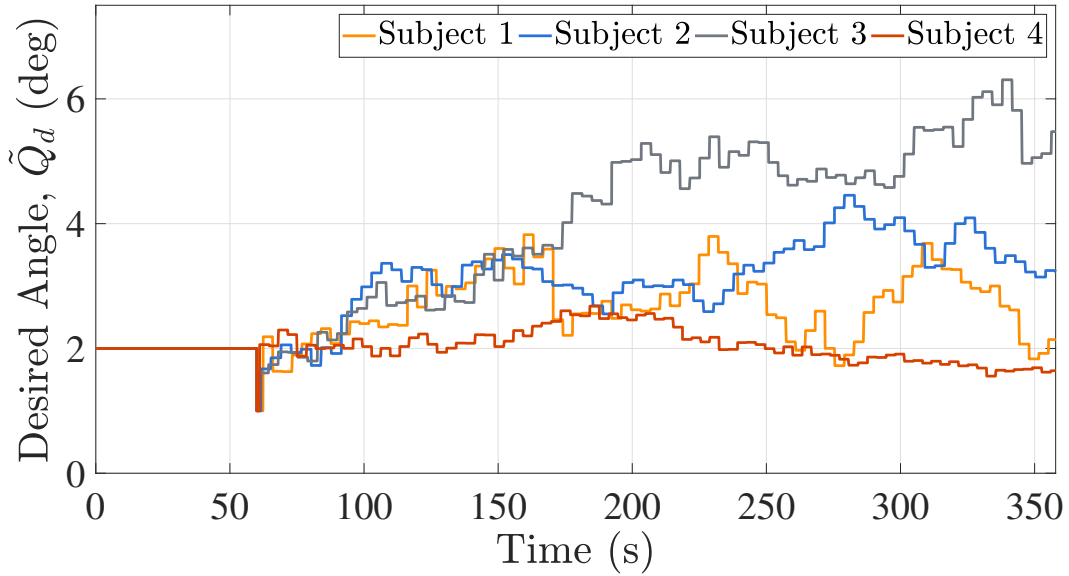


Figure 3.4: The desired, perturbation angle denoted as \tilde{Q}_d is the median of Q_d computed in (3.2) for all subjects. The evolution of the perturbation magnitudes is shown for the duration of the experiments. Perturbations with a magnitude of two degrees are first applied for the initial 60 seconds of all experiments (for familiarization) and then ESC algorithm is activated with an initial condition of 1 degree.

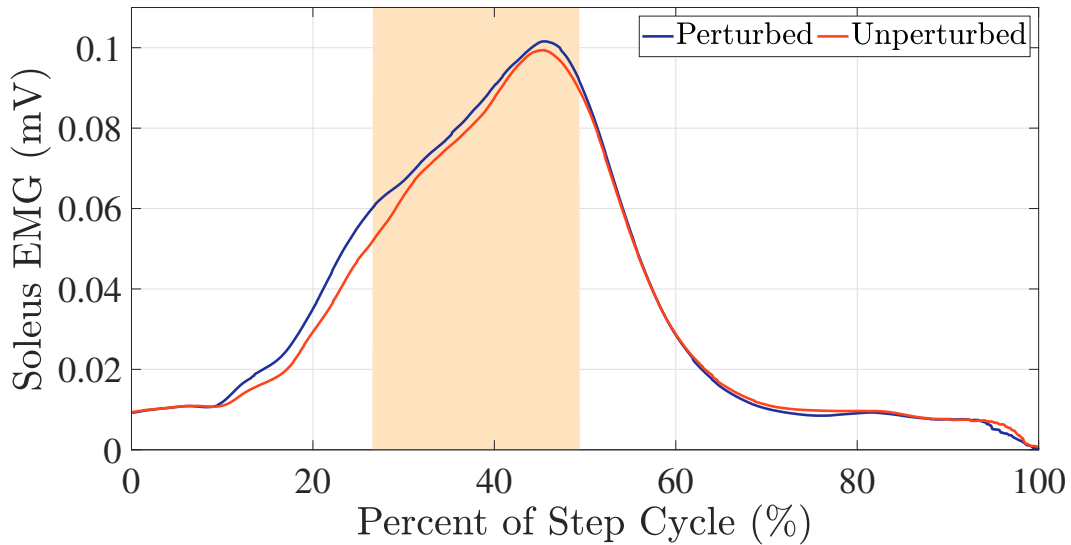


Figure 3.5: The rectified and filtered average soleus muscle response as a function of the step cycle of ESC perturbed (blue) and unperturbed (orange) walking steps for subject 1. The shaded region denotes the perturbation region.

The soleus muscle activity was collected to compute the optimal ankle perturbation magnitude via ESC. The increased average response of the soleus muscle for perturbed steps compared to unperturbed steps is depicted in Figure 3.5. The effect of perturbations with the ESC as compared to unperturbed steps is measured as the mean of the soleus muscle activity in the perturbation region over the entire five minutes of perturbed steps as reported in Table 4.1.

Experimental results in four able-bodied individuals were presented to illustrate the feasibility of the developed control methods. Suitable tracking performance is provided leveraging the terminal error, which is the error at the peak dorsiflexion angle. Preliminary evidence that support muscle activity differences between changes perturbed steps (with varying perturbation magnitudes) and unperturbed steps is provided.

Chapter 4

Influence of Vibration Stimuli on the Quadriceps Femoris Muscles During FES-Induced Cycling

In this chapter, the goal is to investigate the effects of vibratory stimuli applied to the quadriceps muscle belly during FES-cycling. A wearable garment with vibratory motors is placed on the surface of the quadriceps concurrently with a single-channel synchronous FES on both legs to examine the active torque produced. This chapter examines the effects of vibration stimuli applied to the quadriceps femoris during dynamic contractions using a similar device as the one developed in [56], which was tested for isometric contractions. Experiments were conducted on four able-bodied individuals to assess the feasibility of the hybrid cycling approach.

4.1. Experimental Protocol

Four healthy subjects (aged 24.25 ± 5.25 years) participated in the study. All the participants had prior experience with similar FES-cycling protocols but not with the application of vibratory stimulus. A pretrial cycling test was conducted on a separate day and prior to the main cycling trials to determine the pulse width of FES for each participant and to prevent influencing the results of the subsequent cycling trials. The pretrial test was performed at 65 revolutions per minute (RPM) with motorized assistance. The pulse width was selected as the minimum value

to evoke an active torque output of 4 N·m. This torque threshold was selected to prevent fast muscle fatigue buildup during the duration of the cycling trials. The selected pulse width for each participant was used during the cycling trials described below. For all cycling trials, the stimulation frequency and current amplitude of FES were fixed at 60 Hz and 80 mA, respectively, as done in other FES-cycling results [11].

At the beginning of each cycling trial, a passive torque test was performed where the electric motor passively rotated the rider's legs [11] at a constant cadence of 65 RPM without FES to obtain an estimate of the rider's passive torque. Thus, the active torque generated by the muscles was determined by subtracting the passive torque estimate from the real-time torque measurements.

$$\tau_{active} = \tau - \tau_{passive} \quad (4.1)$$

The FES-cycling trials with and without vibratory stimuli were conducted for 2 minutes with the electric motor tracking the target cadence using a robust sliding-mode controller. FES-cycling testing included two trials; one trial without vibration (i.e., typical FES-cycling) and another trial with vibration applied on the quadriceps bilaterally. Participants were instructed to avoid providing voluntary contribution during both cycling trials. FES-cycling was assisted by the electric motor to maintain a cadence of 65 RPM. Vibration was applied concurrently with FES only. A period of 24-72 hours was enforced between the sessions for muscle recovery. Each cycling trial started with the electric motor passively bringing the rider to the target cadence for 25 seconds before applying FES and vibration (for the vibration trial).

After reaching the desired cadence, FES was applied in open-loop fashion during all cycling trials only within kinematic efficient regions of the crank cycle for each participant [11]. The logic state variable denoted by $\sigma : \mathcal{Q} \rightarrow \mathcal{S}$, where $\mathcal{S} \triangleq \{RQ, KDZ, LQ\}$ is the set of possible

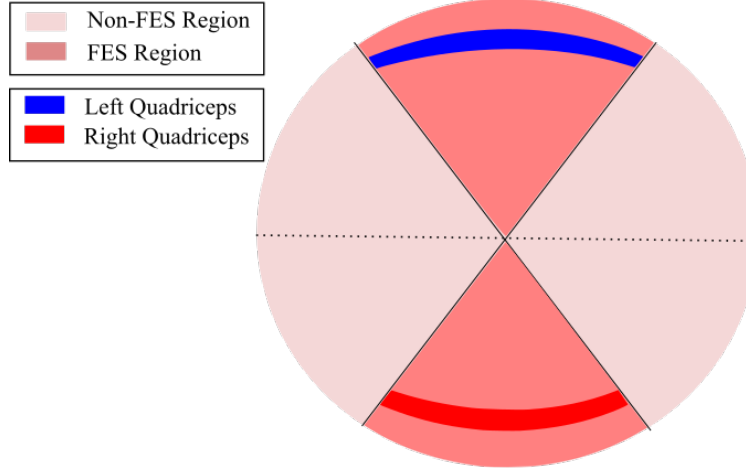


Figure 4.1: Switching signal of FES and motor regions. The FES region is active when $\sigma_m = 1$ such that the quadriceps receive stimulation. The electric motor is active for all time to ensure constant cadence of 65 rpm.

switching subsystems, is defined as

$$\sigma(q) \triangleq \begin{cases} RQ & q \in \mathcal{Q}_r \\ KDZ & q \notin (\mathcal{Q}_r \cup \mathcal{Q}_l), \\ LQ & q \in \mathcal{Q}_l \end{cases}, \quad (4.2)$$

where RQ, LQ denote when the right and left quadriceps are activated, respectively, and the KDZ denotes the kinematic dead zone, where muscles are not activated as they do not evoke significant active torque. Across all subjects, FES was applied within the interval of [66, 157] degrees using the stimulation pattern when $\sigma = 1$ in [57], [58]. The active FES regions (when $\sigma = 1$) is illustrated in Figure 4.1.

4.2. Results

For all trials, data collection started at the point at which the motor brought the rider to the target cadence. The active torque was computed and stored only during the crank angles where FES

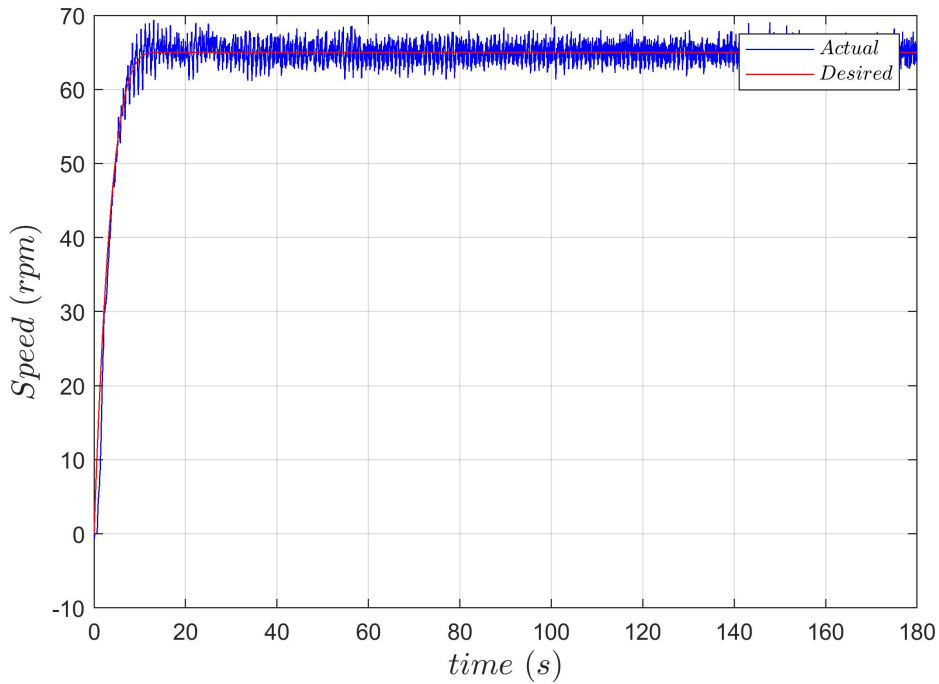


Figure 4.2: The cadence for the duration of one trial. The electric motor assisted FES-cycling to maintain a cadence of 65 RPM.

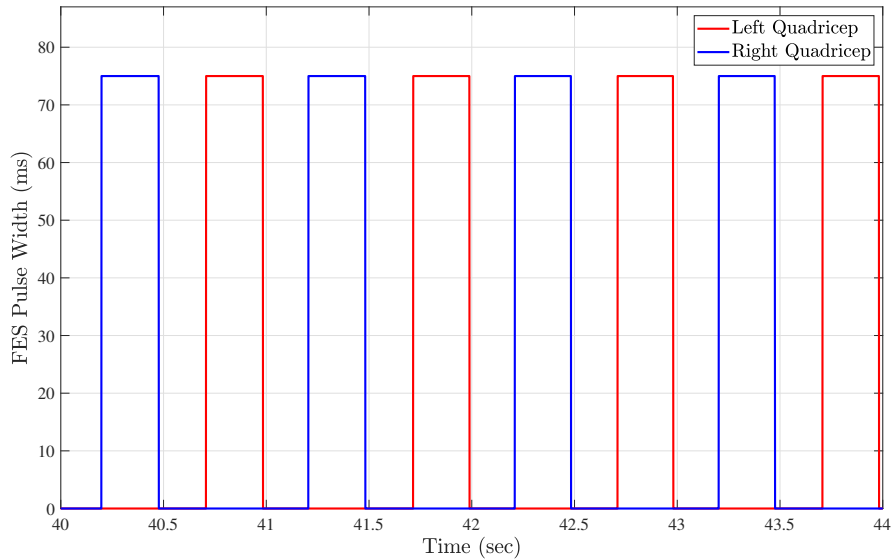


Figure 4.3: The FES command of the left and right quadriceps stimulation patterns. FES was applied only within the kinematic efficient regions. The stimulation frequency and current amplitude of FES were fixed at 60 Hz and 80 mA, respectively. The pulse width was selected to evoke 4 N*m. The pulse width was remained constant between experiment trials.

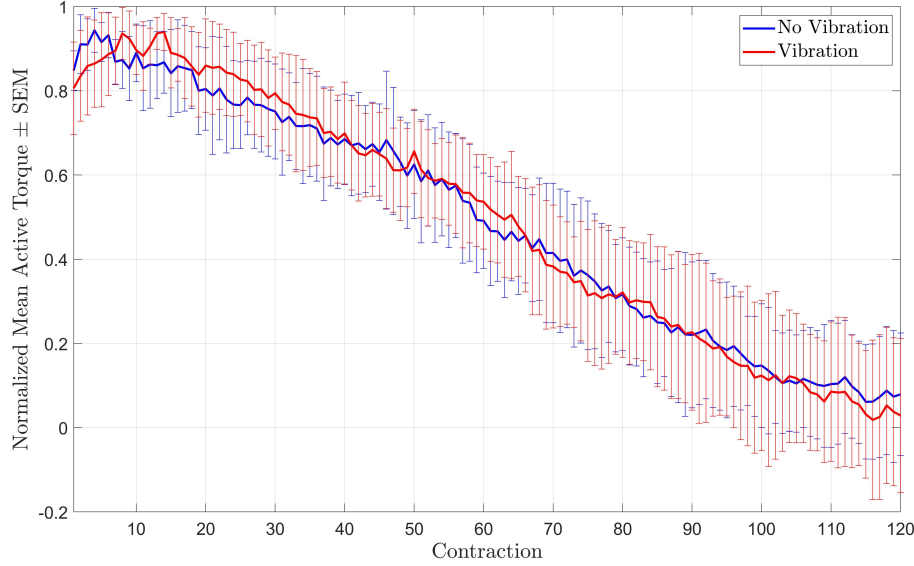


Figure 4.4: Each data point represents the mean value of the active torque over all participants. The maximum torque for each participant was achieved at a different number of contractions. SEM stands for the standard error of the mean.

was applied (i.e., FES regions). A contraction is the average of the active torque of FES regions happening twice every cycle. The mean active torque for every contraction was averaged with a moving window of 1-second; it was then normalized by the maximum active torque produced during the trial for each participant. The normalized curves for all participants were combined and averaged. Three metrics to assess performance were compared across trials: mean active torque, fatigue time, and fatigue rate.

Fatigue time is the elapsed time between the maximum torque contraction and the contraction at which the torque decreased by 30% of the first contraction (measured in the number of contractions) [56]. Fatigue rate is the slope of the best fit linear curve of the function of torque output over 120 contractions. Figure 4.4 depicts the normalized mean torque of all participants over the contractions displaying each activation of FES.

The normalized active torque is shown in Figure 4.4 as a function of contractions for the four participants during both cycling trials. Mean active torque, fatigue rate and fatigue times are presented for each participant (including the used pulse width) in Table 4.1 for the FES-cycling

trials with and without vibration along with the first and third quartile (Q1 and Q3), respectively.

Table 4.1: Mean active torque, fatigue time and fatigue rate for the FES-cycling trials with and without vibration across the four subjects. The pulse width used for each subject was kept constant for both cycling trials.

Subject	Pulse Width	Avg. Active Torque		Fatigue Time		Fatigue Rate	
		no vib.	vib	no vib.	vib	no vib.	vib
Subject 1	75	0.49	0.57	42	55	-9.4	-9.4
Subject 2	80	0.45	0.39	41	41	-9.5	-11.3
Subject 3	80	0.53	0.50	28	33	-5.8	-7.2
Subject 4	90	0.57	0.53	35	33	-7.2	-6.3
Q1		0.39	0.48	29.5	31.5	-9.4	-9.4
Median		0.44	0.51	43.0	37.0	-8.8	-7.0
Q3		0.39	0.55	52.5	52.5	-7.3	-6.2

The electric motor achieved satisfactory cadence tracking because there was a difference of 1.76% ($p=0.44$) of standard deviation of cadence between cycling with (0.172) and without (0.169) vibration for all trials. Hence, cadence was consistent during all cycling trials. There were no statistically significant differences of mean active torque between the cycling trials with and without vibration. The study only tested 4 healthy young subjects (e.g., data set was limited) and a rest period of 24-72 h was used to prevent muscle fatigue to influence the cycling trials. Hence, a potential different trend can be obtained with the recruitment of individuals with SCI and randomizing the order of the trials. Fatigue rates were linearized for best fit ($R^2= 0.98$). The mean fatigue rate for all participants was 5.23% greater for the trial with vibration than the trial without vibration. However, fatigue rates highly varied across participants. The trial with vibration yielded 10.75% lower standard deviation of the active torque than the trial without vibration. This can be interpreted as vibration reducing the variance of active torque output compared to the no vibration trial.

The effects of vibration on muscle fatigue is explored in this chapter. Future work will also include modeling and analysis of the fatigue rates during cycling as in [59], exploring vibration to ease painful sensation for FES applications, and the optimization of vibration and electrical

stimulation parameters will be explored for different cycling cadences.

Chapter 5

Conclusion and Research Directions

In chapter 3, a closed-loop robust controller was developed to track a perturbation trajectory updated by an ESC algorithm to apply ankle joint perturbations within the mid-late stance phase of walking. The ankle perturbations are applied to evoke increments in activity of the soleus muscle during treadmill walking. The robust controller included feedback terms to compensate for the effects of exogenous disturbances and upper bounds of the uncertainties in the dynamic model. Experimental results in four able-bodied individuals were presented to illustrate the feasibility of the developed control methods. Suitable tracking performance is provided leveraging the terminal error, which is the error at the peak dorsiflexion angle. Preliminary evidence supporting muscle activity differences between changes perturbed steps (with varying perturbation magnitudes) and unperturbed steps is provided. Future work includes the implementation of the closed-loop controller and ESC algorithm in stroke survivors during walking.

In chapter 4, further evidence of torque facilitation or depression (i.e., increased or reduced torque) due to the effect of the vibratory stimuli during FES-cycling is to be obtained with a larger sample size. The effects of vibration on muscle fatigue and spasticity in individuals with SCI also remains to be investigated. Future work will also include modeling and analysis of the fatigue rates during cycling as in [59]. Exploring vibration to ease painful sensation for FES applications is also to be explored. The optimization of vibration and electrical stimulation parameters will be explored for different cycling cadences.

The experiments conducted in this thesis were developed to demonstrate the feasibility of the developed control methods. Future work will involve validating these methods in clinical studies. This is likely to present additional control challenges due to reduced muscle mass and strength, faster rates of muscle fatigue, and spasticity.

References

- [1] K. D. Anderson, “Targeting recovery: Priorities of the spinal cord-injured population,” *J. Neurotrauma*, vol. 21, no. 10, pp. 1371–1383, 2004.
- [2] A. J. Del-Ama, A. D. Koutsou, J. C. Moreno, *et al.*, “Review of hybrid exoskeletons to restore gait following spinal cord injury,” *J. Rehabil. Res. Dev.*, vol. 49, no. 4, pp. 497–514, 2012.
- [3] M. Grimmer, R. Riener, C. J. Walsh, *et al.*, “Mobility related physical and functional losses due to aging and disease - A motivation for lower limb exoskeletons,” *J. Neuroeng. Rehabil.*, vol. 16, no. 1, pp. 1–21, 2019.
- [4] L. Marchal-Crespo and D. J. Reinkensmeyer, “Review of control strategies for robotic movement training after neurologic injury,” *J. Neuroeng. Rehabil.*, vol. 6, no. 1, 2009.
- [5] T. G. Hornby, D. S. Reisman, I. G. Ward, *et al.*, “Clinical practice guideline to improve locomotor function following chronic stroke, incomplete spinal cord injury, and brain injury,” *J. Neurol. Phys. Ther.*, vol. 44, no. 1, pp. 49–100, Jan. 2020.
- [6] G. Stampacchia, M. Olivieri, A. Rustici, *et al.*, “Gait rehabilitation in persons with spinal cord injury using innovative technologies: an observational study,” *Spinal Cord*, 2020.
- [7] C. Wiesener and T. Schauer, “The Cybathlon RehaBike: Inertial-Sensor-Driven Functional Electrical Stimulation Cycling by Team Hasomed,” *IEEE Robot. Autom. Mag.*, vol. 24, no. 4, pp. 49–57, 2017.

- [8] H. R. Berry, C. Perret, B. A. Saunders, *et al.*, “Cardiorespiratory and power adaptations to stimulated cycle training in paraplegia,” *Med. Sci. Sports Exerc.*, vol. 40, no. 9, pp. 1573–1580, 2008.
- [9] L. Griffin et al., “Functional Electrical Stimulation Cycling Improves Body Composition, Metabolic and Neural Factors in Persons with Spinal Cord Injury,” *J. Electromyogr. Kinesiol.*, vol. 19, no. 4, pp. 614–622, 2009.
- [10] A. Frotzler, S. Coupaud, C. Perret, *et al.*, “High-volume FES-cycling partially reverses bone loss in people with chronic spinal cord injury,” *Bone*, vol. 43, no. 1, pp. 169–176, 2008.
- [11] C. Cousin, V. Duenas, C. Rouse, *et al.*, “Closed-loop cadence and instantaneous power control on a motorized functional electrical stimulation cycle,” *IEEE Trans Control Sys Tech*, vol. 28, no. 6, pp. 2276–2283, Nov. 2020.
- [12] G. Lv, H. Zhu, and R. D. Gregg, “On the design and control of highly backdrivable lower-limb exoskeletons: A discussion of past and ongoing work,” *IEEE Control Syst.*, vol. 38, no. 6, pp. 88–113, 2018.
- [13] A. J. Young and D. P. Ferris, “State of the Art and Future Directions for Lower Limb Robotic Exoskeletons,” *IEEE Trans. Neural Syst. Rehabil. Eng.*, vol. 25, no. 2, pp. 171–182, Feb. 2017.
- [14] M. Gandolla, E. Guanziroli, A. D. Angelo, *et al.*, “Automatic setting procedure for exoskeleton-assisted overground gait: Proof of concept on stroke population,” *Front. Neurorob.*, vol. 12, no. 10, Mar. 2018.
- [15] D. A. Winter, *Biomechanics and Motor Control of Human Movement*. New York: Wiley, 1990.
- [16] E. J. Rouse, H. Lee, and H. I. Krebs, “Summary of human ankle mechanical impedance during walking,” *IEEE J. Transl. Eng. Health Med.*, vol. 4, pp. 1–7, 2016.

- [17] A. K. Thompson, C. R. Gill, W. Feng, *et al.*, “Operant down-conditioning of the soleus h-reflex in people after stroke,” *Front. Rehabilit. Sci.*, vol. 3, 2022.
- [18] A. L. Hall, C. L. Peterson, S. A. Kautz, *et al.*, “Relationships between muscle contributions to walking subtasks and functional walking status in persons with post-stroke hemiparesis,” *Clin. Biomech.*, vol. 26, no. 5, pp. 509–515, 2011.
- [19] N. Rubino, E. Lawler, J. Casas, *et al.*, “Backstepping control of a motorized ankle orthosis targeting the soleus muscle during walking,” *IFAC-PapersOnLine*, vol. 56, no. 2, pp. 4484–4489, 2023, 22nd IFAC World Congress.
- [20] M. Krstic and H.-H. Wang, “Stability of extremum seeking feedback for general nonlinear dynamic systems,” *Automatica*, vol. 36, no. 4, pp. 595–601, Apr. 2000.
- [21] S. Kumar, A. Mohammadi, D. Quintero, *et al.*, “Extremum seeking control for model-free auto-tuning of powered prosthetic legs,” *IEEE Trans. Control Syst. Tech.*, vol. 28, no. 6, pp. 2120–2135, 2020.
- [22] X. T. Zhang, D. M. Dawson, W. E. Dixon, *et al.*, “Extremum seeking nonlinear controllers for a human exercise machine,” *IEEE Trans. Mechatron.*, vol. 11, pp. 233–240, 2006.
- [23] V. H. Duenas, C. A. Cousin, C. A. Rouse, *et al.*, “Extremum seeking control for power tracking via functional electrical stimulation,” *IFAC-PapersOnLine*, vol. 51, no. 34, pp. 164–169, 2019, 2nd IFAC Conference on Cyber-Physical and Human Systems CPHS 2018.
- [24] N. A. Maffuletti, “Physiological and methodological considerations for the use of neuromuscular electrical stimulation,” *Eur J Appl Physiol*, vol. 110, no. 2, pp. 223–234, Dec. 2010.
- [25] C. M. Gregory, W. E. Dixon, and C. S. Bickel, “Impact of varying pulse frequency and duration on muscle torque production and fatigue,” *Muscle Nerve*, vol. 35, no. 4, pp. 504–509, Apr. 2007.

- [26] C. Wiesener and T. Schauer, “The Cybathlon RehaBike: Inertial-Sensor-Driven Functional Electrical Stimulation Cycling by Team Hasomed,” *IEEE Robot. Autom. Mag.*, vol. 24, no. 4, pp. 49–57, 2017.
- [27] B. M. Doucet, A. Lam, and L. Griffin, “Neuromuscular electrical stimulation for skeletal muscle function,” *Yale J Biol Med*, vol. 85, no. 2, pp. 201–215, Jun. 2012.
- [28] A. S. Gorgey, C. D. Black, C. P. Elder, *et al.*, “Effects of electrical stimulation parameters on fatigue in skeletal muscle,” *J Orthop Sports Phys Ther*, vol. 39, no. 9, pp. 684–692, 2009.
- [29] C. Bickel, C. Gregory, and J. Dean, “Motor unit recruitment during neuromuscular electrical stimulation: A critical appraisal,” *Eur J Appl Physiol*, vol. 111, pp. 2399–2407, 2011.
- [30] T. Lundeberg, R. Nordemar, and D. Ottoson, “Pain alleviation by vibratory stimulation,” *Pain*, vol. 20, no. 1, pp. 25–44, Sep. 1984.
- [31] J. Rittweger, “Vibration as an exercise modality: How it may work, and what its potential might be,” *Eur J Appl Physiol*, vol. 108, no. 5, pp. 877–904, 2010.
- [32] S. Rodríguez-Jiménez, A. Benítez, M. A. García-González, *et al.*, “Effect of vibration frequency on agonist and antagonist arm muscle activity,” *Eur J Appl Physiol*, vol. 115, no. 6, pp. 1305–1312, Jun. 2015.
- [33] M. A. Cardinale and J. Lim, “Electromyography activity of vastus lateralis muscle during whole-body vibrations of different frequencies,” *J Strength Cond Res*, vol. 17, no. 3, pp. 621–624, 2003.
- [34] M. Roelants, S. M. Verschueren, C. Delecluse, *et al.*, “Whole body vibration induced increase in leg muscle activity during different squat exercises,” *J Strength Cond Res*, vol. 20, no. 1, pp. 124–129, 2006.
- [35] L. L. Ness and E. C. Field-Fote, “Effect of whole-body vibration on quadriceps spasticity in individuals with spastic hypertonia due to spinal cord injury,” *Restor Neurol Neurosci*, vol. 27, no. 6, pp. 623–633, 2009.

- [36] S. Cerciello, S. Rossi, E. Visona, *et al.*, “Clinical applications of vibration therapy in orthopaedic practice,” *Muscles Ligaments Tendons J*, vol. 6, no. 1, pp. 147–156, 2016.
- [37] F. H. Magalhães, D. Rezende de Toledo, and A. F. Kohn, “Plantar flexion force induced by amplitude-modulated tendon vibration and associated soleus v/f-waves as evidence of a centrally-mediated mechanism contributing to extra torque generation in humans,” *J NeuroEng Rehabil*, vol. 10, no. 32, 2013.
- [38] M. A. Gorassini, D. J. Bennett, and J. F. Yang, “Self-sustained firing of human motor units,” *Neurosci Lett*, vol. 247, no. 1, pp. 13–16, May 1998.
- [39] J. Roll, J. Vedel, and E. Ribot, “Alteration of proprioceptive messages induced by tendon vibration in man: A microneurographic study,” *Exp Brain Res*, vol. 76, no. 1, pp. 213–222, 1989.
- [40] P. D. Gail, J. Lance, and P. Neilson, “Differential effects on tonic and phasic reflex mechanisms produced by vibration of muscles in man,” *J Neurol Neurosurg Psychiatry*, vol. 29, no. 1, pp. 1–11, Feb. 1966.
- [41] B. A. DeForest, J. Bohorquez, and M. A. Perez, “Vibration attenuates spasm-like activity in humans with spinal cord injury,” *J Physiol*, vol. 598, no. 13, pp. 2703–2717, 2020.
- [42] N. Murillo, H. Kumru, J. Vidal-Samso, *et al.*, “Decrease of spasticity with muscle vibration in patients with spinal cord injury,” *Clinical neurophysiology : official journal of the International Federation of Clinical Neurophysiology*, vol. 122, no. 6, pp. 1183–1189, 2011.
- [43] L. Espeit, V. Rozand, G. Y. Millet, *et al.*, “Influence of wide-pulse neuromuscular electrical stimulation frequency and superimposed tendon vibration on occurrence and magnitude of extra torque,” *J. Appl. Physiol*, 2021.
- [44] F. H. Magalhães and A. Kohn, “Vibration-induced extra torque during electrically-evoked contractions of the human calf muscles,” *J Neuroeng Rehabil*, vol. 7, no. 26, pp. 1–16, 2010.

- [45] R. Riener, F. Ferrarin, E. E. Pavan, *et al.*, “Patient-driven control of FES-supported standing up and sitting down: Experimental results,” *IEEE Trans. Rehabil. Eng.*, vol. 8, no. 4, pp. 523–529, 2000.
- [46] T. Schauer, N. O. Negård, F. Previdi, *et al.*, “Online identification and nonlinear control of the electrically stimulated quadriceps muscle,” *Control Eng. Pract.*, vol. 13, no. 9, pp. 1207–1219, Sep. 2005.
- [47] F. L. Lewis, D. M. Dawson, and C. T. Abdallah, *Robot Manipulator Control*. 2003, p. 638.
- [48] N. Mazzaro, M. J. Grey, and T. Sinkjær, “Contribution of afferent feedback to the soleus muscle activity during human locomotion,” *J. Neurophysiol.*, vol. 93, no. 1, pp. 167–177, 2005.
- [49] J. B. Andersen and T. Sinkjaer, “Mobile ankle and knee perturbator,” *IEEE Trans. Biomed. Eng.*, vol. 50, no. 10, pp. 1208–1211, 2003.
- [50] M. Guay, “A perturbation-based proportional integral extremum-seeking control approach,” *IEEE Transactions on Automatic Control*, vol. 61, no. 11, pp. 3370–3381, 2016.
- [51] J. Yang, R. Stein, and K. James, “Contribution of peripheral afferents to the activation of the soleus muscle during walking in humans,” *Experimental Brain Research*, vol. 87, pp. 679–687, 1991.
- [52] G. L. Gottlieb and G. C. Agarwal, “Response to sudden torques about ankle in man: Myotatic reflex,” *Journal of Neurophysiology*, vol. 42, no. 1, pp. 91–106, 1979.
- [53] S. Kumar, A. Mohammadi, R. D. Gregg, *et al.*, “Limit Cycle Minimization by Time-Invariant Extremum Seeking Control,” *Proceedings of the American Control Conference*, pp. 2359–2365, 2019.
- [54] A. F. Filippov, “Differential equations with discontinuous right-hand side,” in *Fifteen papers on differential equations*, ser. American Mathematical Society Translations - Series 2, vol. 42, American Mathematical Society, 1964, pp. 199–231.

- [55] N. Fischer, R. Kamalapurkar, and W. E. Dixon, “LaSalle-Yoshizawa corollaries for nonsmooth systems,” *IEEE Trans. Autom. Control*, vol. 58, no. 9, pp. 2333–2338, Sep. 2013.
- [56] V. Duenas, C. Cousin, R. Downey, *et al.*, “Influence of vibration stimuli on neuromuscular electrical stimulation of the quadriceps femoris muscle group,” *IFESS*, 2016.
- [57] V. H. Duenas, C. A. Cousin, A. Parikh, *et al.*, “Motorized and Functional Electrical Stimulation Induced Cycling via Switched Repetitive Learning Control,” *IEEE Trans. Control Syst. Technol.*, vol. 27, no. 4, pp. 1468–1479, 2019.
- [58] M. J. Bellman, T. H. Cheng, R. J. Downey, *et al.*, “Switched Control of Cadence during Stationary Cycling Induced by Functional Electrical Stimulation,” *IEEE Trans. Neural Syst. Rehabil. Eng.*, vol. 24, no. 12, pp. 1373–1383, 2016.
- [59] C. Fornusek and G. Davis, “Maximizing muscle force via low-cadence functional electrical stimulation cycling,” *Taylor and Francis Health Sciences*, pp. 232–237, 2004.

Chapter 6

Vita

Evan Tulsky is expected to receive a bachelor's degree in Mechanical Engineering in 2024 from Syracuse University. He has attended and presented a conference proceeding (Chapter 4) at the International Functional Electrical Stimulation Society (IFESS) at Rehab Week in September 2021. The published abstract paper can be found in the March 2022 edition of the Artificial Organs Journal IFESS section on page E77. Further, he has a work under submission (Chapter 3) to an internal conference sponsored by the IEEE control systems society. He is expected to join the Bionics Systems Control Lab (BSC) research group at Syracuse University to pursue his doctoral degree under the supervision of Dr. Victor H. Duenas in Fall 2024.

6.1. Publications

Tulsky, ER, Casas, J, Cheng-Hao, C, Brose, S, Duenas, V. (September, 2021). "Influence of Vibration Stimuli Applied on the Quadriceps Femoris Muscles During Functional Electrical Stimulation Induced Cycling", International Functional Electrical Stimulation Society, Rovinj, Croatia (Online).